Nitrogen-doped bamboo-like carbon nanotubes with Ni encapsulation for persulfate activation to remove emerging contaminants with excellent catalytic stability

Jian Kang[a], Xiaoguang Duan[a], Chen Wang[a], Hongqi Sun[b,]*, Xiaoyao Tan[c], Moses O. Tade[a], and Shaobin Wang[a,]*

[a]Department of Chemical Engineering, Curtin University, GPO Box U1987, Perth, WA6845, Australia

[b]School of Engineering, Edith Cowan University, Joondalup, WA 6027, Australia.

[c]State Key Laboratory of Hollow Fibre Membrane Materials and Processes, Department of Chemical Engineering, Tianjin Polytechnic University, 399 Binshui West Road, Tianjin 300387, China

*Corresponding authors
Tel: +61 8 9266 3776. E-mail: shaobin.wang@curtin.edu.au (S. Wang)
Tel: +61 8 6304 5067. E-mail: h.sun@ecu.edu.au (H. Sun)

ABSTRACT

Nitrogen-doped bamboo-like carbon nanotubes encapsulated with nickel nanoparticles (Ni@NCNTs) were feasibly fabricated by a one-pot pyrolysis route. The characterization techniques revealed the surface morphology, structure and chemical composition of the as-prepared catalysts synthesized in different conditions. Ni@NCNTs were employed as both adsorbents and catalysts for activating persulfate to remove an emerging pollutant, antibiotic sulfachloropyridazine. The nitrogen modification enhanced both adsorption capacity and catalytic ability of Ni@NCNTs and proved to be a promising alternative to metal oxides and other carbon catalysts. Moreover, Ni@NCNTs showed an excellent stability because of nitrogen heteroatom doping and Ni nanoparticle encapsulation. Electron paramagnetic resonance (EPR) and classical radical quenching tests discovered a simultaneous radical/non-radical mechanism in Ni@NCNTs/persulfate system. The results indicated that the novel nano-architectured catalyst materials can show emerging functionalities for environmental remediation processes.

Keywords: Nitrogen doping, carbon nanotubes, antibiotics, persulfate, sulfate radicals

1. INTRODUCTION

Worldwide drinking water scarcity has become more intense because of the wide water contaminations, which appears as one of the most critical challenges in the world. Many water treatment techniques have been employed to cope with the rapid deterioration of water pollution in terms of the discharge quantity and ever-increasing complexity [1]. Recently, emerging contaminants, for instance pharmaceuticals and personal care products (PPCPs), have attracted tremendous attention. Their intrinsic properties, the continuous and fast development of new species, ubiquity in all surface waters, difficulty of complete remediation and tardy action in early days, as well as lack of understanding of their possible jeopardization to the environment, have brought out great issues to the development of remediation technologies [2, 3].

As a representative and main contributor of PPCPs, sulfonamide antibiotics have been intensively used in animal husbandry and human medicine owing to their low cost and good therapeutic effect [4-8]. As a pharmaceutical product, sulfonamides are extremely recalcitrant to complete natural biodegradation because they are biological active [9]. Many studies have detected various sulfonamide compounds in aqueous environment. Even at a low level, a continuous and long-term exposure to such chemicals could lead to appreciable adverse effects on human health [10]. Therefore, the complexity, fine water solubility and trace amount have made them difficult to reach complete degradation via traditional wastewater treatment measures in wastewater treatment plants (WWTP) [11, 12]. Recently, advanced oxidation processes (AOPs) have attracted massive attention as they are very effective for the degradation and mineralization of refractory organic pollutants in the aquatic environment [13]. Typically, AOPs are involving oxidants and superoxides such as ozone, oxygen, hydroperoxide, and various radicals that are capable of destroying target organics to harmless species. Hydroxyl radicals ($^{\bullet}$OH) have been most consequently observed in AOPs such as Fenton reaction, UV oxidation and ozonation owing to their superior oxidation ability towards organic pollutants with almost no selectivity [14, 15]. Yet, the drawbacks of many $^{\bullet}OH$-related Fenton-like reactions, such as excess sludge production, narrow pH (~3) requirement and metal leaching, are the bottleneck limits. Comparably, strong oxidizing sulfate radical ($SO_4^{\bullet-}$) offers an excellent alternative to hydroxyl radical ($^{\bullet}OH$) because $SO_4^{\bullet-}$ has a higher oxidation potential (2.5–3.1 V) than hydroxyl radicals (2.7 V) and a better flexibility of pH tolerance [15-17]. Analogous to Fenton-like oxidation reactions, sulfate radicals can be obtained by activating persulfate (PS) through various activation methods, such as UV-light irradiation, heating, carbon catalysis, metal ion and metallic oxide catalysis, for organic contaminant degradation [18-21]. Among the catalysts used in AOPs, carbon-based nanomaterials stand out owing to the exceptional adsorption capacity, catalysis ability and environmentally friendly nature [22]. Graphene oxide, reduced graphene oxide, carbon nanotubes, and nanodiamonds have been employed in water treatment as an excellent alternative to metal-based catalysts and shown great competitiveness in terms of avoiding metal toxics and associated contamination [23]. However, pristine carbocatalysts suffer from poor stability in heterogeneous reactions, and the heteroatom doping with N, S, P or B into carbon honeycomb network offers an effective strategy to tackle such an issue [24-32].

Herein, we demonstrate a one-pot facile synthesis of high quality N-doped carbon nanotubes with nickel nanoparticle encapsulation (Ni@NCNTs) via direct pyrolysis of melamine as carbon/nitrogen co-precursor and nickel chloride as a Ni source. The prepared product presented a high N-doping level (6.6%) and successful Ni encapsulation. In addition, due to the synergistic effect of N-doping and Ni decoration, the catalytic oxidation and reusability were dramatically enhanced comparing with CNT and N-CNT in activation of PS to effectively remove sulfachloropyridazine (SCP) in water. Electron paramagnetic resonance (EPR) and quenching tests were used to investigate the mechanism of PS activation and SCP oxidation.

2. EXPERIMENTAL

2.1 Chemicals and materials

Nickel chloride hexahydrate ($NiCl_2{\bullet}6H_2O$, 98%), phenol (99%), sulfachloropyridazine (99%), 5, 5-dimethyl-1-pyrroline (DMPO), Potassium persulfate, and hydrochloride acid (32%) were obtained from Sigma-Aldrich. Multi-walled carbon nanotubes (MWCNTs) were purchased from Timesnano, China. Graphene oxide (GO) was prepared via a modified Hummers' approach and reduced graphene oxide (rGO) was fabricated by annealing the obtained GO in a tubular furnace under nitrogen atmosphere at 700 ^{o}C for 1 h. Nitrogen doped reduced graphene oxide (N-rGO) was prepared through a hydrothermal approach, as detailed in previous studies [32-34]. All the chemicals were of analytical grade or higher and used as received without further purification. Deionized (DI) water was used in all the experiments.

2.2 Synthesis of nitrogen-doped carbon nanotubes with nickel encapsulation (Ni@NCNTs)

Nitrogen-doped carbon nanotubes with nickel encapsulation were fabricated by a controlled pyrolysis process using melamine and nickel chloride hexahydrate as carbon/nitrogen and nickel precursors, respectively. In a typical synthesis, melamine ($C_3N_6H_6$, 10 g) were dissolved in 20 mL of DI water at 65 ^{o}C under continuous stirring for 1 h until melamine was dissolved completely. $NiCl_2{\bullet}6H_2O$ as a nickel precursor with designed loading (1, 2, 3.3, or 7 g) was introduced to the melamine solution to form a homogenous greenish solution. Later, the mixed solution was heated and kept at 80 ^{o}C overnight to completely remove water. The resulting precipitates were placed inside a tube furnace and allowed nitrogen gas to flow through for three hours to purge out the air residue. And then the samples were annealed at 700, 800 or 900 ^{o}C for 6 h under N_2 atmosphere with a heating rate of 5 ^{o}C min^{-1}. After the pyrolysis, the sample was naturally cooled down to room temperature. Finally, the resultant black product was ground to fine powders, followed by thoroughly washing with excessive concentrated hydrochloride acid (32%), by stirring in the acid solution for 6 h. The obtained precipitates were then washed with ethanol and DI water for a few times until the clear solution pH achieved at the value of 7. The as-prepared catalysts were denoted as Ni@NCNT-T-M (where T represents the calcination temperature and M represents the initial weight ratio of melamine to nickel chloride), for instance Ni@NCNT-700-3 means Ni@NCNTs with 3:1 melamine to $NiCl_2{\bullet}6H_2O$ and heated at 700 ^oC.

2.3 Catalyst characterization

The crystal structure of the samples determined by X-ray powder diffraction patterns were recorded on a Bruker D8 Advance X-ray diffractometer using Cu Kα radiation (λ = 1.5406 Å) at 40 mA and 40 kV with a scanning speed of 0.2° (2θ) min^{-1}. The Raman spectra were obtained using a laser with an excitation wavelength of 785 nm at room temperature on a Renishaw Raman microscope. The surface contents and types of carbon, nitrogen and metals were measured by X-ray photoelectron spectroscopy (XPS) on a VG Multi lab 2000 spectrometer (Kratos AXIS Ultra DLD) with Al Kα radiation as the X-ray source (300 W). The C 1s line at 284.6 eV was applies as a calibration to correct the binding energies. By deducting the Shirley-type background, the core level spectra were deconvoluted into their components with Gaussian-Lorentzian (20:80) shape lines using the CasaXPS software. The Brunauer−Emmett−Teller (BET) specific surface area and pore-size distribution of the samples were determined by N_2 adsorption−desorption at −196 °C using a Micrometrics Tristar 3000. The samples were degassed in a vacuum at 110 °C overnight before the tests. The morphologies of the carbon samples were characterized using scanning electron microscopy (SEM; FEI Verios XHR 460) and transmission electron microscopy (TEM; JEOL 2100). The thermal stability was collected by the thermogravimetric analysis (TGA) using a TGA/DSC1 STAR^e system, Mettler-Toledo thermal analyzer under flowing air. The reactive radicals were detected by electron paramagnetic resonance (EPR) on a Bruker EMS-plus instrument with DMPO as a spin-trapping agent, and the Xeon software (Bruker) was used to analyze the quantitative information. The Ni concentration in reaction solutions was evaluated by an Inductively Coupled Plasma Optical Emission Spectrometer (ICP-OES).

2.4 Adsorption and catalytic oxidation of SCP solutions

SCP adsorption was performed in a 500 mL conical flask at 25 °C, unless other temperature specifically mentioned. Typical adsorption experiments were carried out by dispersing the

Ni@NCNTs samples (0.2 g L^{-1}) in SCP (20 mg L^{-1}, pH = 7) solutions. At determined intervals, 1 mL of solution was withdrawn and immediately filtered by a 0.22 μm Millipore syringe filter to remove the solid particles.

2.5 Catalytic oxidation of SCP solutions

The degradation experiments were conducted by introducing designed amount of PS into the reaction solutions when the adsorption/desorption equilibrium was reached. After the reaction was initiated, 1 mL of solution was extracted at planned time intervals, and then injected into an UHPLC vial mixed with 0.5 mL methanol as the quenching agent. Each experiment and analysis was repeated twice and the results were reproducible with relative errors less than ± 5%. The concentrations of SCP were analyzed with an UHPLC system (Thermo-Fisher Scientific 3000) using an UV detector at a detection wavelength of 270 nm. An Acclaim RSLC C-18 column (2.2 μm) was used as a separation column. The mobile phase was a mixture of diluted acetic acid and methanol (70:30, v/v) with a flow rate of 0.3 mL min^{-1} and 20 μL of injection volume [32]. Total organic carbon (TOC) was measured using a Shimadzu TOC-5000 CE analyzer for a few selected samples. For TOC measurement, 10 mL sample was withdrawn at a designed interval, filtered and quenched with 10 mL of 0.3 M sodium nitrite solution, and then the mixed solution was analyzed [35]. Data reported in the figures are mean values of at least three experiments with error bars representing the standard deviation.

3. Results and discussion

3.1 Characterization of carbon nanotubes materials

X-ray diffraction (XRD) was employed to investigate the crystalline structure of the prepared CNTs. **Fig. 1** displays the XRD spectra of CNT, N-CNT and Ni@NCNTs composites synthesized at various pyrolysis temperatures. All the carbon nanotubes showed a broad reflection peak at $2\theta = 26.5^{o}$, corresponding to the (002) plane of graphitic carbon with an interlayer spacing of 0.34 nm. The peak intensity increased when temperature elevated from 700 to 800 ^{o}C and then decreased at 900 ^{o}C.

Additionally, the XRD spectra of Ni@NCNTs of different nitrogen loading amounts are shown in **Fig. S1**. It is noticed that the broad background band centred at 2θ =26^o might be owing to the successful incorporated nitrogen defects in the graphitic structure [36]. Aside from the graphitic carbon peak, three pronounced peaks can be observed at 2θ = 44.5, 51.9 and 76.4^o, corresponding to the (111), in comparison with CNT and N-CNT, (200) and (311) reflections of Ni nanoparticles, respectively and confirming the incorporation of Ni nanoparticles in the CNT catalysts [37]. A less conspicuous peak appearing at 41^o indicated the existence of nickel carbide (Ni_3C) in the CNTs. It is worth to notice that there is no obvious nickel oxide peak detected, typically at around 2θ = 37^o, which might be attributed to the reduction of nickel ions to nickel nanoparticles by carbon atoms. It was found that nickel ions could be reduced to nickel metal nanoparticles by using amorphous carbon as a reductant in argon atmosphere at 500 ^{o}C and that nickel oxide particles could be reduced by natural graphite at a high pyrolysis temperature [38] [39]. Moreover, the CNT compartment layers may also provide the embedded nickel particles a protection shell from being oxidized.

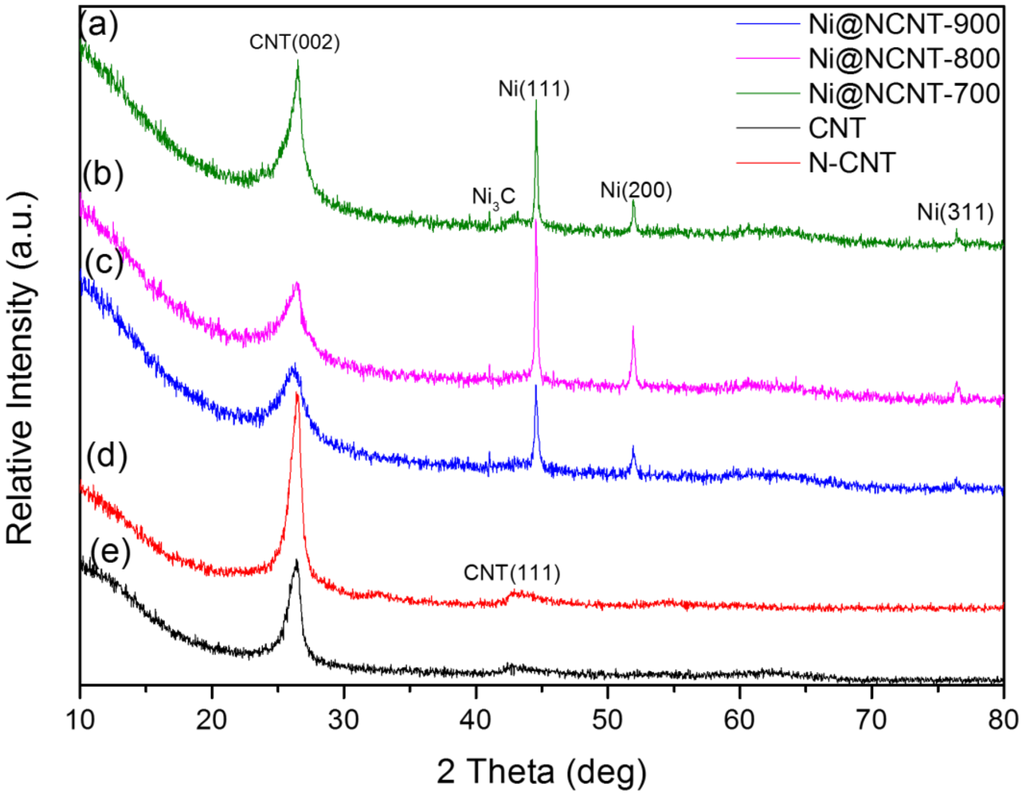

Fig. 1 XRD patterns of (a) Ni@NCNT-900-3, (b) Ni@NCNT-800-3, (c) Ni@NCNT-700-3, (d) N-CNT, (e) modified CNT samples.

Raman spectroscopy as one of the most sensitive and informative techniques is widely used to evaluate graphitic materials for graphitization degree, graphene layer number or carbon nanotube wall layers, nanotube diameter, disorder level in sp^2 network and doping grade. **Fig. 2** shows the Raman spectra of Ni@NCNTs at various pyrolysis temperatures, e.g. 700, 800 and 900 °C, CNT and N-CNT. Three prominent peaks are observed at 1330, 1573 and 2648 cm^{-1}, which are attributed to the D, G and 2D bands, respectively.

The intensity ratio of D band to G band (I_D/I_G) is often used to evaluate the structural disorder of carbon materials. The I_D/I_G of N-CNT (1.38) showed higher value than modified CNT (1.29), indicating that nitrogen doping on the sp^2 carbon network could largely boost the defect density. The I_D/I_G ratio of Ni@NCNTs decreases from 1.33 to 1.22 with increasing pyrolysis temperature from

700 to 900 °C, suggesting that the carbon nanotubes possess less lattice defects and disorders derived from high pyrolysis temperature. The disorder property of the catalysts will be further confirmed by electron microscopy. The G band peak width is another indicator of heteroatom doping [40] [41]. **Fig.2** shows that G band width of CNT synthesized at various temperatures came along with an order of Ni@NCNT-700 > Ni@NCNT-800 > Ni@NCNT-900, confirming the successful N doping, and that the doping degree reduced with elevated pyrolysis temperature. **Fig. S2** also shows the variation of I_D/I_G ratio along with the nitrogen precursor weight percentage, indicating that a higher nitrogen precursor content would give rise to a higher N doping level. However, when the nitrogen and nickel precursors loading ratio was raised to 7, the I_D/I_G ratio dropped, suggesting that higher nitrogen precursor amount would not always give a higher disorder level.

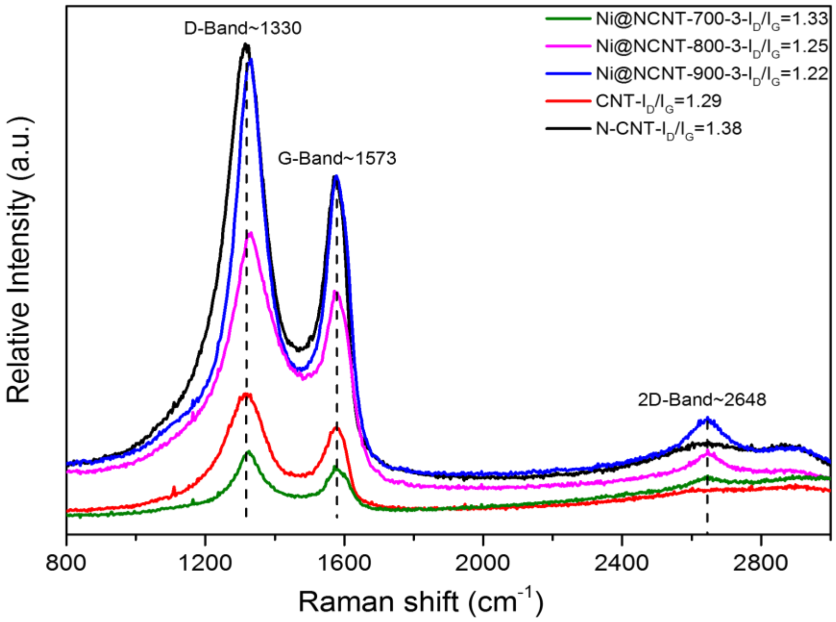

Fig. 2 Raman spectra of Ni@NCNTs at different annealing temperatures, CNT and N-CNT.

The surface morphology of the as-synthesized Ni@NCNTs nanostructures was characterized by SEM and TEM imaging. The SEM images in **Fig. 3(a)** reveal that the product fabricated at 800 °C contains well grown nanotubes with a herringbone structure and is free from impurities such as amorphous carbon and polyhedral carbon particles. The diameter of the tubes ranges from 70 to 400 nm, and length can be up to dozens of micrometres. TEM images in **Figs. 3(b)** and (c) further confirm that they are hollow CNTs with a typical bamboo-like and compartmentalized structure. It was also shown that the pea-pod like nickel particles are encapsulated inside the carbon tubes. The inner tube diameter and the wall thickness of a typical carbon nanotube were measured to be 45 and 20 nm, respectively. In addition, it was observed that most of the nickel nanoparticles were kept inside the CNTs after being washed in concentrated hydrochloride acid solution for hours, indicating that the nickel nanoparticles are quite inaccessible from being affected by outside environment, acid solution and oxidation. To further confirm such a point, **Fig. 3(d)** shows the morphology of CNTs before acid treatment. The nickel particles (black dots) are randomly dispersed over the CNTs both inside and outside. On the other hand, the acid treated tubes in **Fig. 3(b)** show a nice and clean tube surface. Many metal-based catalysts have been extensively applied for AOPs, yet the metal leaching is surely a barrier for their further development [29]. In this study, the Ni content of Ni@NCNTs/PS reaction solutions was tested by ICP-OES and it was shown that the Ni concentration was as low as 0.47 mg L^{-1}, which is within the limit of nickel range 0.02 – 1 mg L^{-1} of the world drinking water quality [42]. In addition, the magnetic property of Ni@NCNTs before and after acid wash is shown in **Fig. S3**. The raw Ni@NCNT showed strong magnetism, and the magnetism was largely reserved even after acid wash, which is due to the carbon layers on Ni particles. Such magnetic property can be very convenient for post catalyst recycling process.

In **Fig. 3(e)**, nickel particles are detected at the tip of the CNTs, which implies that a tip-growth mechanism might be responsible for the formation of carbon nanotube. Besides, the motion trail of nickel particles is illuminated in **Fig. 3(f)**, suggesting that the nickel particles are able to diffuse along the tube axis and aggregate at the tube end to form a worm-like Ni catalyst lump. A magnified TEM image of encapsulated nickel particles is shown in **Fig. 3(e) (inset)**. The nickel nanoparticles are embedded in a graphitic shell composing of well-ordered carbon layers, and the inter plane spacing of the fringe lattices is in a range from 0.34 to 0.38 nm, which increased with growing tube diameter and agreed to the size effect’s rule [43].

In order to systematically study the influences of the pyrolysis temperature and amount of nitrogen precursor on CNTs morphology and microstructure, the SEM images of CNTs synthesized at different conditions are displayed in **Fig.S4**. At 700 ºC, the obtained sample represents a chrysanthemum-like carbon nanotube cluster with irregular tube sizes and short length, also the graphene like carbon material can be observed (**Figs. S4** and **S5**). As the SEM image was taken from the overlook-angle, one can clearly see that many of the growing tubes are observed to be open ended and interestingly showing a multi-walled carbon tube structure, which is consistent with the Raman results.

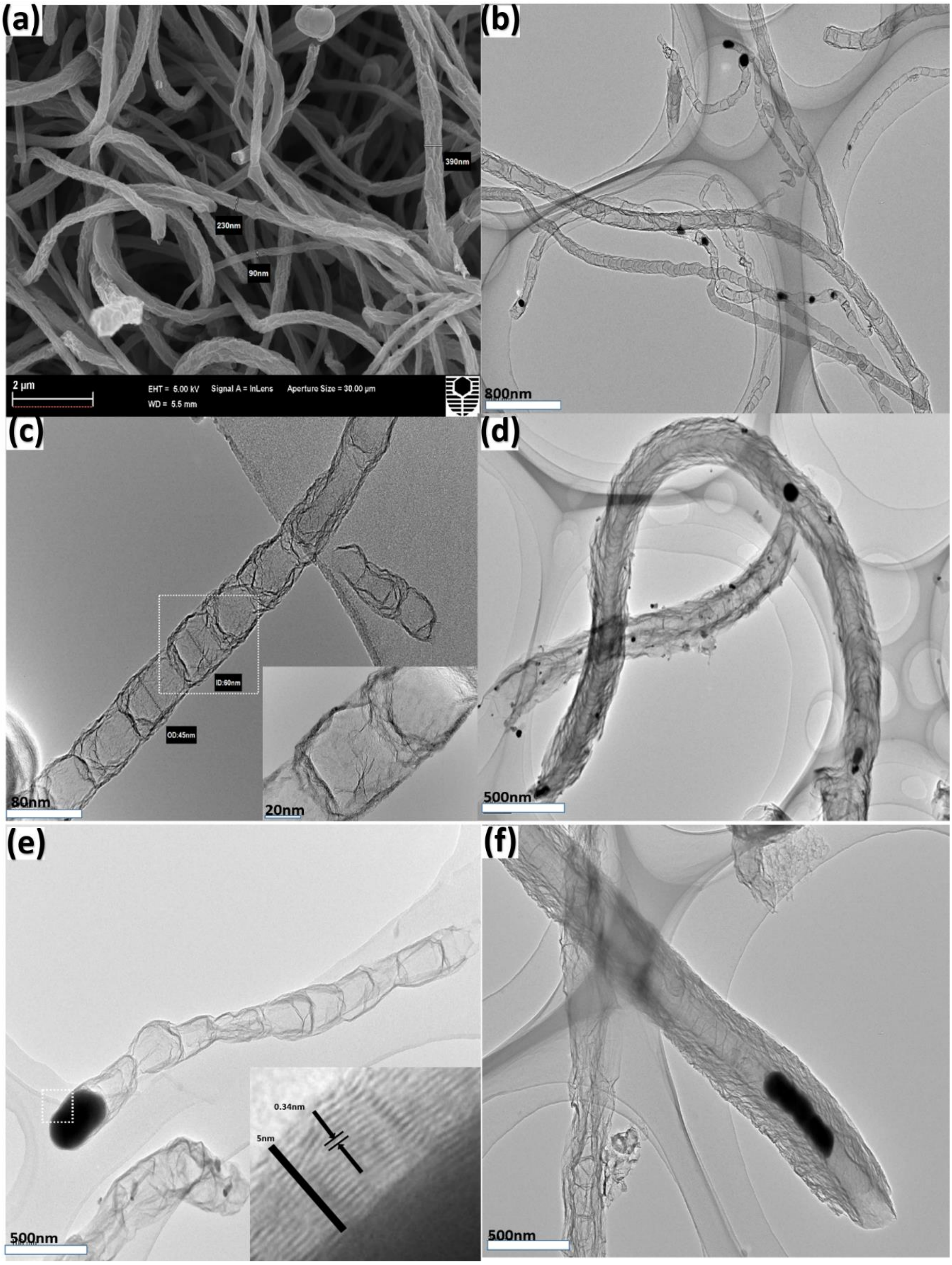

Fig. 3 SEM and TEM characterization of the Ni encapsulated N-doped carbon nanotube. (a) SEM image of the Ni@NCNT-800-3. (b) TEM image of Ni@NCNT-800-3 with pea-pod like Ni particle encapsulation. (c) TEM images of bamboo like CNT structure with compartments; inset shows the magnified part of the compartments. (d) TEM image of Ni@NCNT-800-3 before acid treatment. (e)

TEM image of Ni@NCNT-800-3 with tip Ni encapsulation; inset displays the graphitic layers of the carbon shell. (f) TEM image of Ni@NCNT-800-3 with worm like Ni particle accumulation at the tube end.

The chemical composition and state of the nitrogen doped carbon nanotubes were analyzed by XPS. **Fig.4** displays the XPS survey showing C 1s, N 1s, O 1s and Ni 2p spectra. The emergence of N 1s peak in all samples confirmed that nitrogen atoms were successfully doped into carbon catalysts. Moreover, the XPS element analysis shows the N doping levels are 9.12%, 6.59% and 5.15% in Ni@NCNTs synthesized at 700, 800 and 900 ^{o}C, respectively, which are superior to many other reported approaches such as physical vapor deposition (PVD) of 3.5% and chemical vapor deposition (CVD) of 4%. [31, 44] The high nitrogen doping level also indicated that melamine as an excellent nitrogen precursor can efficiently incorporate nitrogen atoms into carbon nanotube network during the CNTs formation process. Table S1 shows the N doping levels in Ni@NCNTs at different synthesis conditions.

The chemical states of different types of N dopants were studied by high resolution of N1s spectrum in a specific range (392-408 eV). **Fig. 4(b)** illustrates the N1s spectrum was deconvoluted into four types of N peaks, 398.9, 401.1, 402.7 and 405.2 eV, corresponding to pyridinic N (N at the edges of the graphene layers bonded to two carbon atoms), pyrrolic N (N in five-membered rings), graphitic N or quaternary N (N in six-membered rings within the graphene layers) and oxidized N, respectively. **Fig. 4(c)** shows that the graphitic N content gradually increased from 8.67 to 10.38% with elevated temperature, 700 to 900 ^{o}C. This may be due to the better thermal stability of graphitic N and the loss of unstable N at high temperature [45-49]. The oxygen and nickel contents in these samples are also listed in Table S1. All the samples represented a very low oxygen content due to pyrolysing in the inert gas atmosphere at a high temperature, which enables most of the oxygen containing groups to react with carbon to form CO_X. The XPS C 1s spectra are shown in **Fig. S6**. The thermal stability of the typical Ni@NCNTs was investigated by TGA-DSC (**Fig. S7**). A total of 32% of the initial weight was remaining which can be nickel compounds such as NiO and Ni_2O_3, at Ni content of roughly 22%.

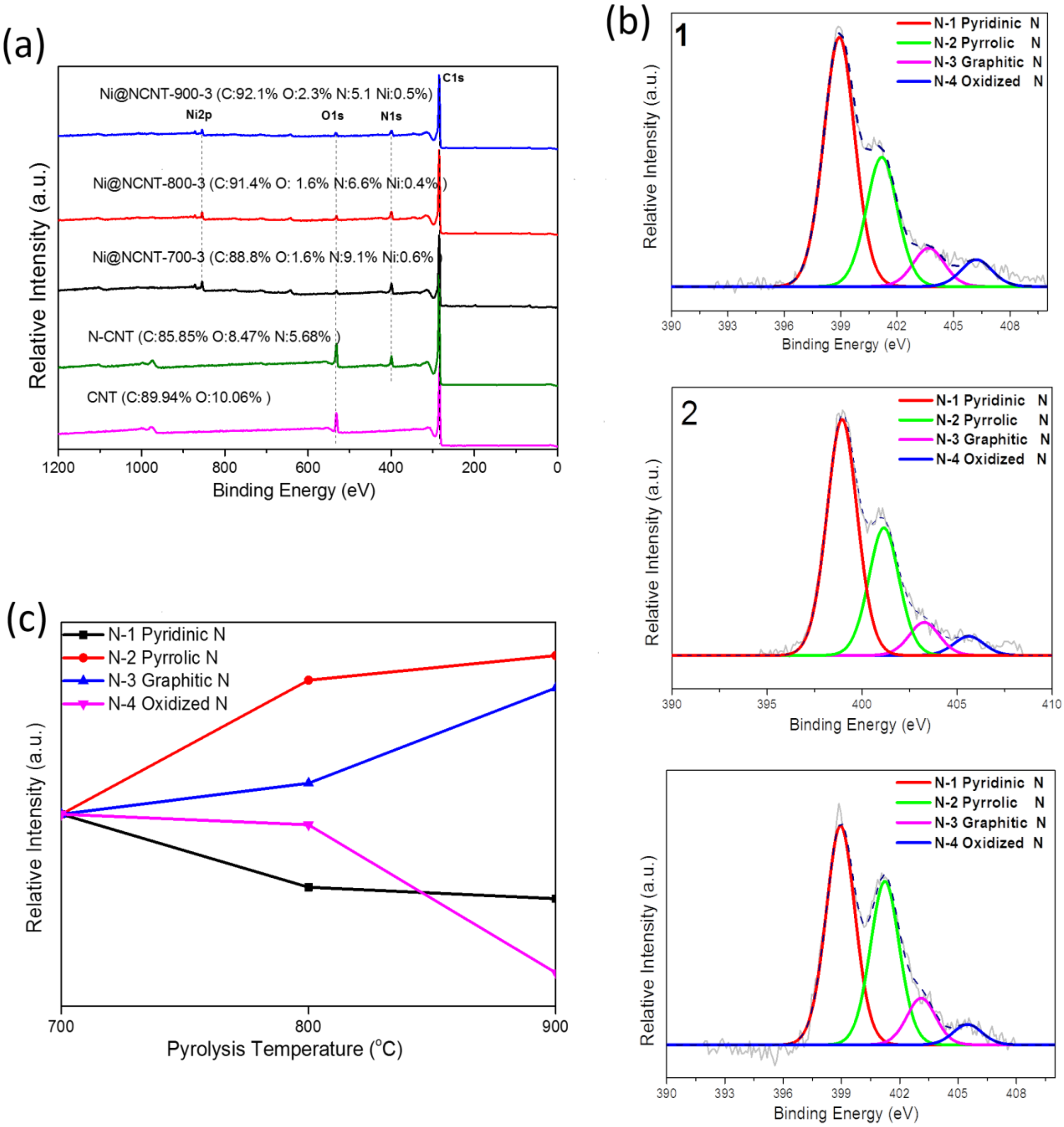

Fig. 4 (a) XPS survey of Ni@NCNT-700, Ni@NCNT-800, Ni@NCNT-900, CNT and N-CNT. (b) N 1s scan of 1. Ni@NCNT-700, 2. Ni@NCNT-800 and 3. Ni@NCNT-900. (c) Density change of N components at different temperatures.

Fig.5 shows the BET specific surface areas and pore structure of the as-synthesized samples at various fabrication temperatures. All the samples demonstrated a type IV isotherm with a H3 hysteresis loop that gradually increases at low pressure followed by a sharp jump at half way, illuminating the mesoporous structure [50]. The hysteresis loop of each sample in **Fig.5 (a)** shows quite a similarity, Ni@NCNT-800-3 was slightly broader than the other two, suggesting a higher N doping content would create more defect sites and lead to a more porous structure with a greater surface area and pore volume (Table S2). The catalysts fabricated at 700 ^{o}C had a smaller surface area (135 m^2/g) than 800 ^{o}C (155 m^2/g). But at 900 ^{o}C the BET (145 m^2/g) declined due to the collapse and aggregation of carbon nanotube. The pore size distribution (PSD) of samples is displayed in **Fig.5 (b)**, in which a sharp peak appears in all the three catalysts at 2.2, indicating that the Ni@NCNTs are mostly composed of micropores (< 2 nm) and mesopores (2-50 nm).

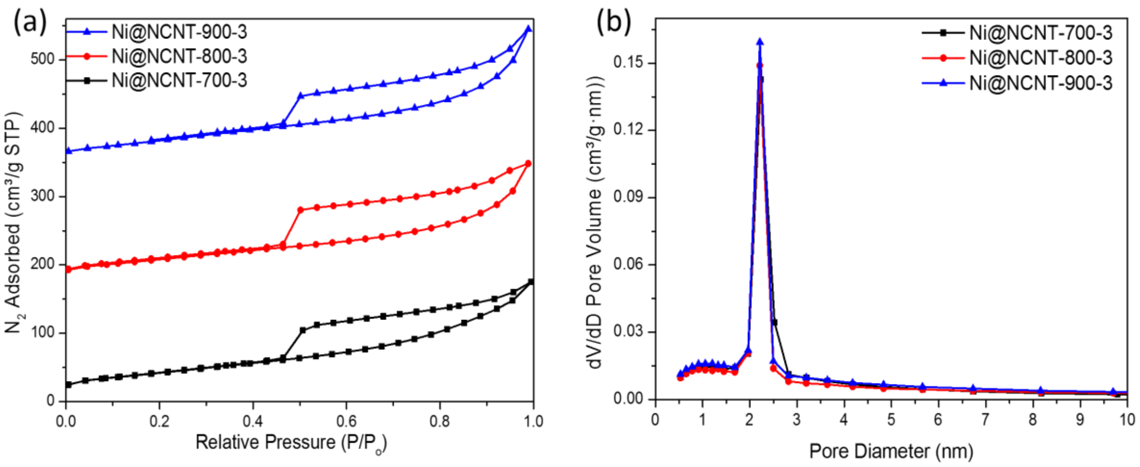

Fig.5 (a) Nitrogen sorption isotherms and (b) pore size distributions of Ni@NCNTs at various synthesising temperatures.

3.2 Catalytic SCP removal performance of carbon nanotubes

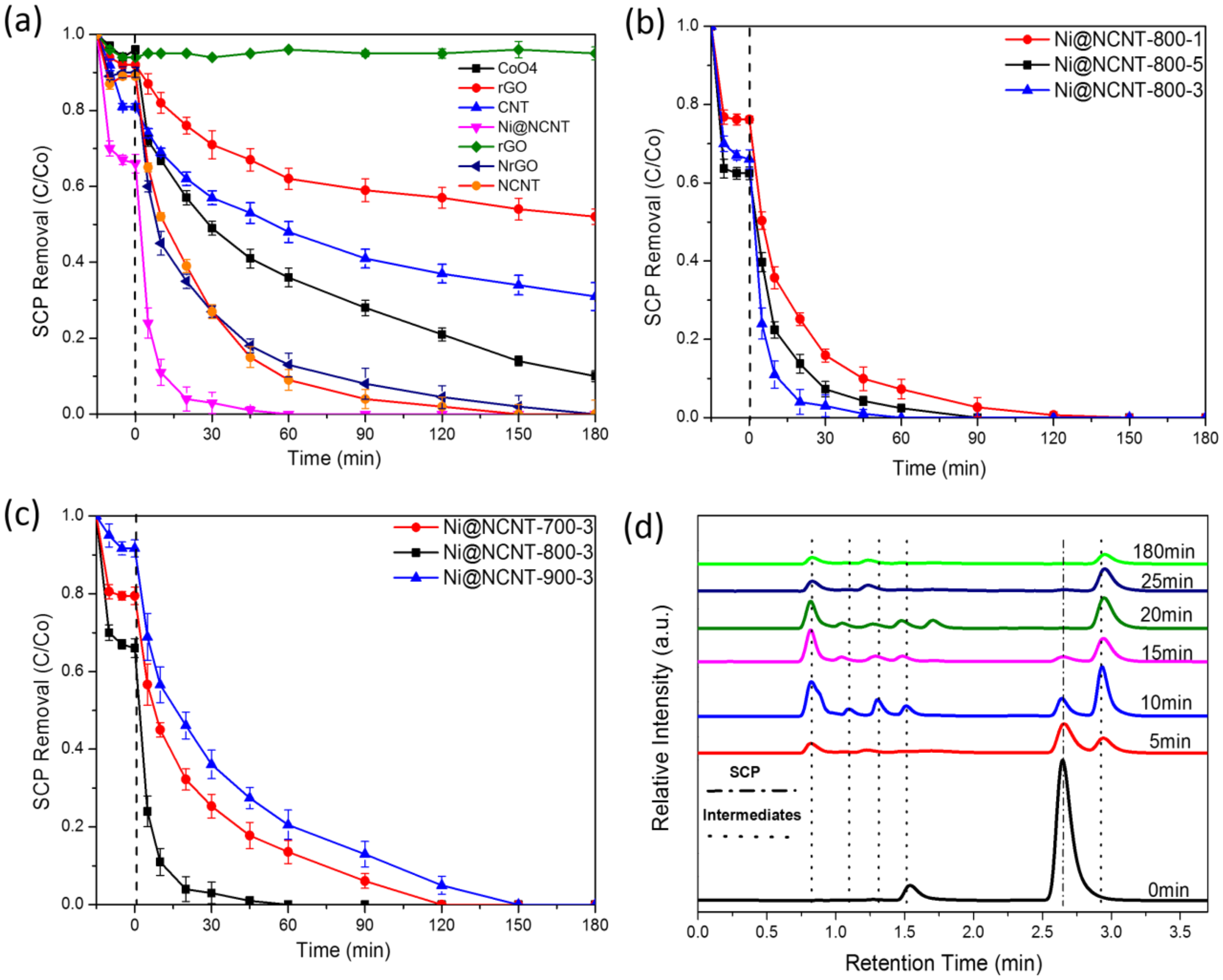

Fig. 6 (a) PS activation over various catalysts. (b) Effect of nitrogen/nickel precursor loading of Ni@NCNT-800 on SCP removal. (c) Effect of catalyst fabrication temperature on SCP removal. (d) HPLC spectra of SCP degradation in a 180 min experiment. (Initial SCP concentration = 20 mg/L, catalyst loading = 0.2 g/L, PS concentration = 2 g/L, and temperature at 25 $^{\mathrm{o}}$C.)

Comparative studies of various carbocatalysts and metal oxides were first carried out in catalytic activation of PS for SCP oxidation in aqueous solutions. Before the PS was introduced into the solution, a 15-min pre-adsorption was performed in order to distinguish the SCP removal achieved by adsorption. When PS was added individually, a limited amount of SCP removal (< 5%) was reached, suggesting that PS could barely oxidize SCP compounds without catalytic activation. Both rGO and N-rGO showed low adsorption of SCP, however, the catalysis of N-rGO was greater than rGO. As our previous studies demonstrated, N doping could remarkably improve the carbocatalytic activity by enhancing the π- π bond of the carbon matrix through the lonely pair of electrons of doped nitrogen atoms [27, 30, 32]. In this study, a similar case occurred. Comparing the catalysis on modified commercial CNT, NCNT and as-prepared Ni@NCNT-800-3, MWCNT only reached less than 65% of SCP removal and NCNT presented a higher activity than CNT, giving SCP removal at 100% in 3 h while Ni@NCNT-800-3 achieved 100% SCP oxidation efficiency within 1 h, indicating that the N doping and Ni encapsulation induced catalytic enhancement. Nickel nanoparticles were also tested for SCP degradation, but showing much less activity (10%). Moreover, Co_3O_4 as a typical metal based catalyst was employed to compare with the as-prepared Ni@NCNTs on PS activation. **Fig.6(a)** shows that Co_3O_4 presented a poor adsorption capacity and a moderate catalytic activity at 5% SCP adsorption and around 90% oxidation in 180 min, respectively, indicating that Ni@NCNTs is more effective than the conventional metal oxide and other carbon catalysts for PS activation.

It is believed that a higher N doping level can lead to a more advanced catalysis [51-53]. **Fig. 6(b)** shows the effect of the nitrogen doping level on SCP removal. As shown in Table S1, the nitrogen contents for Ni@NCNT-800-1, Ni@NCNT-800-3 and Ni@NCNT-800-5 are 5.8, 6.6 and 7.7%, respectively. The 15-min pre-adsorption tests show that SCP adsorption capacities are 0.08, 0.11 and 0.13 mol g^{-1} for Ni@NCNT-800-1, Ni@NCNT-800-3 and Ni@NCNT-800-5, respectively. Interestingly, the catalytic ability, however, does not follow the adsorption capacity trend where the reaction rate increases in an order of Ni@NCNT-800-3> Ni@NCNT-800-5 > Ni@NCNT-800-1.

The catalysis of Ni@NCNTs was first improved when the nitrogen content increased from 5.8 to 6.6% and more nitrogen functional groups on the CNT surface would work as active sites. However, when the N doping reached its optimum level, a further increased N doping (7.7%) would cause destruction of graphitic network structure and deterioration of the catalyst activity instead.

The influence of pyrolysis temperature at 700, 800 and 900 °C on catalytic oxidation was investigated (**Fig. 6(c)**). The adsorption capacity and catalytic oxidation of SCP of the three counterparts are in an order of Ni@NCNT-900-3 < Ni@NCNT-700-3 < Ni@NCNT-800-3, where Ni@NCNT-800-3 exhibited the best performance of complete decomposition of SCP in 60 min. This indicates that a higher pyrolysis temperature did not necessarily endow greater catalysis and adsorption. Moreover, SEM images showed that high annealing temperature can trigger the destruction and aggregation of carbon nanotubes, which might be a main reason for the deactivation of Ni@NCNTs. The decay of the SCP during the oxidation process was monitored by UHPLC as illustrated in **Fig. 6(d)**. It can be seen that a well-defined SCP peak appeared at retention time (t_R) = 2.65 min and its peak intensity gradually decreased while a number of by-products were emerged during the oxidation process. The major intermediates include p-aminophenol (PAB), 3-amino-6-chloropyridazine (3A6C), 3-amino-4-hydroxy-6-chloropyridazine (3A4H6C) and 4-amino-3-hydroxybenzenesulfonic acid (4A3H). As the degradation process continues, benzene rings of the SCP by-products could be further degraded to reach ring-opening to form small molecules such as maleic acid, malic acid and oxalic acid, which would be finally decomposed to water and carbon dioxide. A much detailed investigation on SCP degradation will be carried out in the future.

In addition, PS activation rate was also checked on some catalysts. As illustrated in Fig. S8, PS shows continuous decomposition with reaction time. Ni@NCNTs presented high PS decomposition rate than NCNT and Ni@NCNT-800-3 demonstrated a higher PS decomposition rate than other Ni@NCNTs catalysts, which confirms the higher activity of Ni@NCNT-800-3.

To further investigate the mineralization of SCP oxidation, total organic carbon (TOC) was determined (**Fig. S9**). The TOC trend chart is well aligning with UHPLC results that SCP was degreased rapidly in the first 30 min and then became relatively steady and achieved 78% of TOC removal in 180 min, indicating that most of the SCP and its intermediates were oxidized into harmless chemicals such as water and carbon dioxide.

3.3 Effect of several reaction parameters on SCP removal

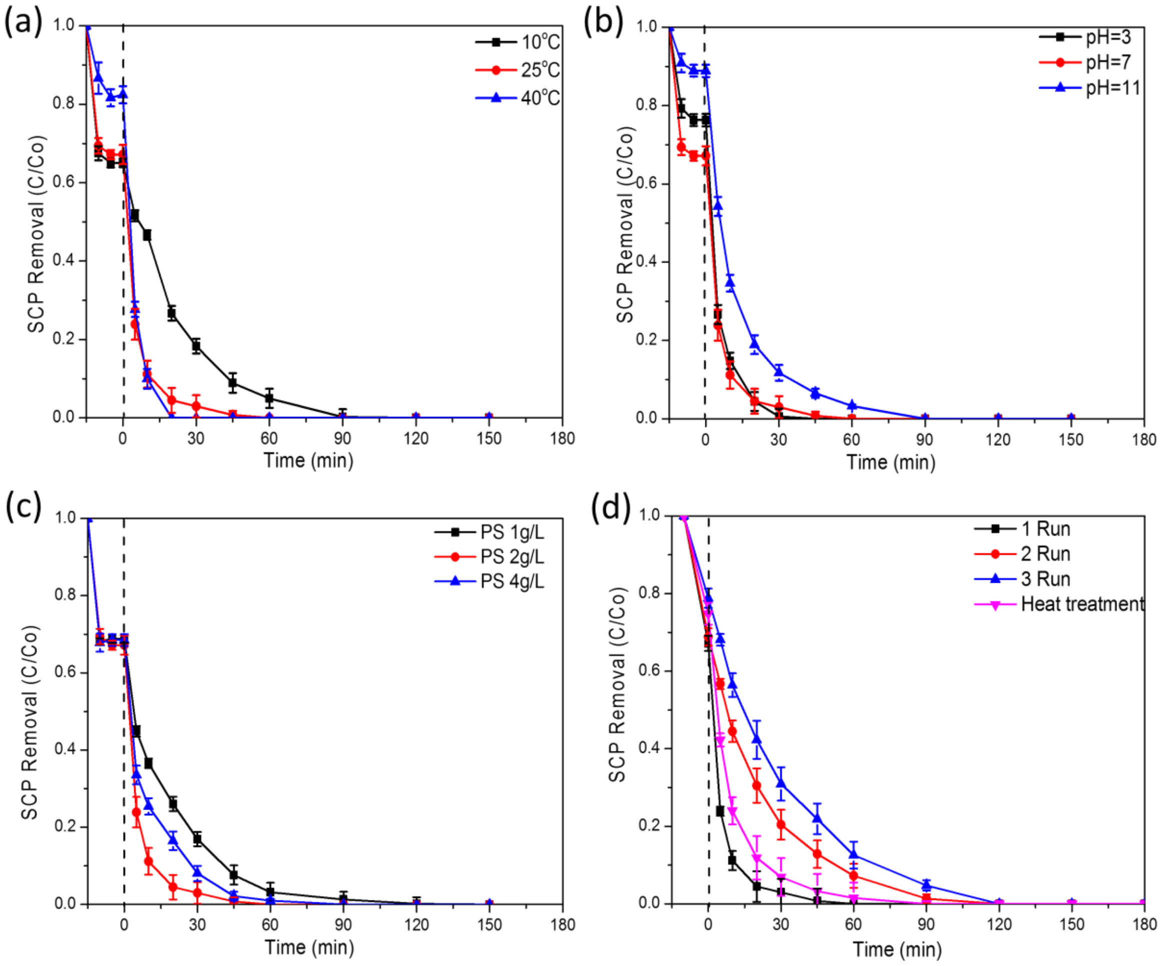

Fig.7 (a) Effect of reaction temperature on SCP removal. (b) Effect of reaction solution pH values on SCP removal. (c) Effect of PS loading on SCP removal. (d) Stability and reusability of Ni@NCNT-800-3. (Unless specific mentioned, initial SCP concentration = 20 mg/L, catalyst loading = 0.2 g/L, PS concentration = 2 g/L, and temperature at 25 °C.)

Fig. 7(a) displays the SCP removal by a synergetic effect of Ni@NCNT-800-3 adsorption and heterogeneous oxidation of PS in a range of 10-40 °C. The change of the solution temperature had a noticeable effect on the adsorption of Ni@NCNT, in an order of 0.06 mol g^{-1} (40 °C) < 0.11 mol g^{-1} (25 °C) < 0.12 mol g^{-1} (10 °C), suggesting a better adsorption ability to SCP at a lower temperature. The complete SCP removal was obtained in 90, 60 and 20 min at 10, 25, and 40 °C, respectively. The reaction rate constants (Table 1) at different temperatures were well fitted by the first-order kinetics

(Eq. 1) with great regression coefficient values ($R^2 = 0.99$) and the activation energy was calculated to be 37.9 kJ mol^{-1} according to the Arrhenius equation. The first order kinetic model is listed below:

$$\ln\left(\frac{C}{Co}\right) = kt \qquad (1)$$

Where k is the reaction constant and C and C_o are the SCP concentrations at reaction time (t)=t and t=0, respectively.

Fig.7(b) shows that Ni@NCNT-800-3 presented the best adsorption (0.11 mol g^{-1}) performance at pH = 7. When pH reached as high as 11, the adsorptive SCP removal dropped. Moreover, it is noted that a complete degradation of the antibiotic SCP was achieved in all three cases, depending on the various solution pH values. The reaction rate constants are k = 0.15, 0.09 and 0.07 min^{-1} for pH = 3, 7 and 11, respectively.

Table 1. Reaction rate constants and activation energy.

Temp °C	*Reaction rate constant: k(min^{-1})*	*Regression coefficients: R^2*	*E_a: Activation energy* kJ mol^{-1}
10	0.04	0.997	
25	0.09	0.997	37.9
40	0.21	0.999	

The influence of PS loading on SCP degradation rate was studied in the range of 1-4 g L^{-1} (**Fig.7(c)**). The change of the PS loading had an effect on the SCP oxidation reaction, the reaction rate constant k varied from 0.05 min^{-1} for 1 g L^{-1} to 0.09 and 0.07 min^{-1} for 2 and 4 g L^{-1}, respectively. Our previous studied have proven that the oxidation reaction rate is consistent with the increase of PS/PMS loading. However, a further adding of PS after the optimum concentration may cause self-quenching reaction, leading to reduced oxidation efficiency [54].

The influence of initial SCP concentration on its degradation is illustrated in Fig. S10. SCP concentration also affects the degradation rate. Higher SCP concentration results in lower degradation efficiency. At 100 ppm, only 93% SCP removal could be achieved in 3 h. This may be due to two main factors. More adsorbed SCP molecules and intermediates would cover the active sites of Ni@NCNT, hindering the activation of PS. Meanwhile, insufficient amount of PS would be a limiting factor for degradation of high concentration of SCP solution.

3.4 Stability tests

The stability and reusability of prepared Ni@NCNTs and modified commercial CNT were tested by similar SCP oxidation experiments after each use and heat treatment at 350 °C in nitrogen atmosphere for 1 h. In **Fig. 7(d)**, Ni@NCNTs showed outstanding stability being able to achieve completely SCP decomposition in 120 min in all four-run tests, where the fresh catalyst completely degraded SCP in 60 min, and recycled catalyst will degrade SCP in 90 and 120 min for the second and third runs, respectively. What more stunning is, after ultrasonic cleaning and heat treatment of the third-run used catalyst, the sample catalysis was recovered showing almost equivalent catalytic ability to the fresh sample. Such good catalysis stability was comparable to or even better than some metal based catalysts [55-57]. The decrease in the second and third runs was mainly due to the changes in surface chemistry and structure of the catalyst. The SSA and pore structures of Ni@NCNTs were reduced after the first run (Table S3). The adsorption of SCP and its intermediates for the coverage of surface active sites will reduce the contact area of Ni@NCNTs and PS, thus leading to the reduction in the catalytic activity. These adsorbed organic molecules can be removed via thermal annealing and the catalytic activity was mostly recovered after the heat treatment. It is not excluded that some of the catalysts were lost during the collection and cleaning processes in recycling runs, resulting in a lower activity in the sequent test. In addition, Ni leaching in the tests was determined (Table S3) and it is found that Ni ion concentrations in the four runs are much low.

Fig. S11 shows the reusability of conventional MWCNT on PS activation for SCP degradation. It decomposed 70% SCP in 180 min in the first run, and the SCP decomposition efficiencies were 49%

and 20% for the second and third runs, respectively. It can be inferred that the nickel encapsulation might be acting as supporting beans inside the nanotubes and prevent the catalyst from collapsing and destructing so that it could maintain good catalysis after numbers of usage. Moreover, the encapsulated Ni particles can accelerate the PS activation efficiency by transferring electrons from the inner Ni metals to the outer carbon tube walls. This effect can be largely conserved due to the carbon wall protection when the catalyst was reused successively.

3.5 EPR studies

In PS activation involved AOPs, it is well accepted that reactive radicals such as sulfate ($SO_4^{-\bullet}$) and hydroxyl radicals ($^{\bullet}OH$) are the predominant active species in attacking organic pollutants [58-60]. Here, EPR was carried out to probe the detailed catalytic oxidation mechanism and identify the reactive species of Ni@NCNTs activating PS for SCP degradation. A spin-trapping agent, 5, 5-dimethylpyrroline-oxide (DMPO), was employed to capture the free radicals in the activation reaction. **Fig. 8(a)** shows that no obvious radical peak was observed without adding DMPO and strong characteristic signals of both $SO_4^{-\bullet}$ and $^{\bullet}OH$ were observed after DMPO introduction. It can be seen that Ni@NCNTs was able to activate PS to generate a high intensity of hydroxyl radicals and relatively lower amount of sulfate radicals throughout the oxidation reaction. Duan *et al*. recently investigated PS activation on phenol oxidation and suggested persulfate molecules can mainly be activated and decomposed to produce $SO_4^{-\bullet}$, yet the generation of hydroxyl radicals were presumably attributed to oxidization of water molecules absorbed on carbocatalyst through a one electron transfer process [60]. The variation of free radical concentration versus time was depicted in **Fig. 8(a)**, PS was able to produce a minor amount of radicals by self-activation without introducing a catalyst, however, the intensities of radical peaks were largely enhanced after Ni@NCNTs catalyst was added and reached the maximum in 10 min, which is well agreed with the change of SCP degradation rate. Moreover, both $SO_4^{-\bullet}$ and $^{\bullet}OH$ showed a minor receding after first 10 min, ascribed to the consumption of SCP oxidation, and then appeared no obvious change afterwards. This can be attributed to the outstanding catalytic ability and stability of Ni@NCNTs that can continue to activate persulfate throughout the reaction. In lateral comparison among Ni@NCNT-800-1, Ni@NCNT-800-3 and Ni@NCNT-800-5, all three catalysts displayed a similar change in radical concentration that increased first and started to reduce after reaching the maximum (**Fig. S12**).

In quenching tests, **Fig. 8(b)** shows that SCP removal efficiency was slightly decreased when ethanol was added at an ethanol/PS molar ratio of 500 and the degradation efficiency kept reducing with increasing addition of ethanol. Interestingly, the SCP solution was still able to reach complete removal in 180 min when the aqueous solution was completely replaced by ethanol, suggesting occurrence of non-radical reactions as all radicals were quenched.

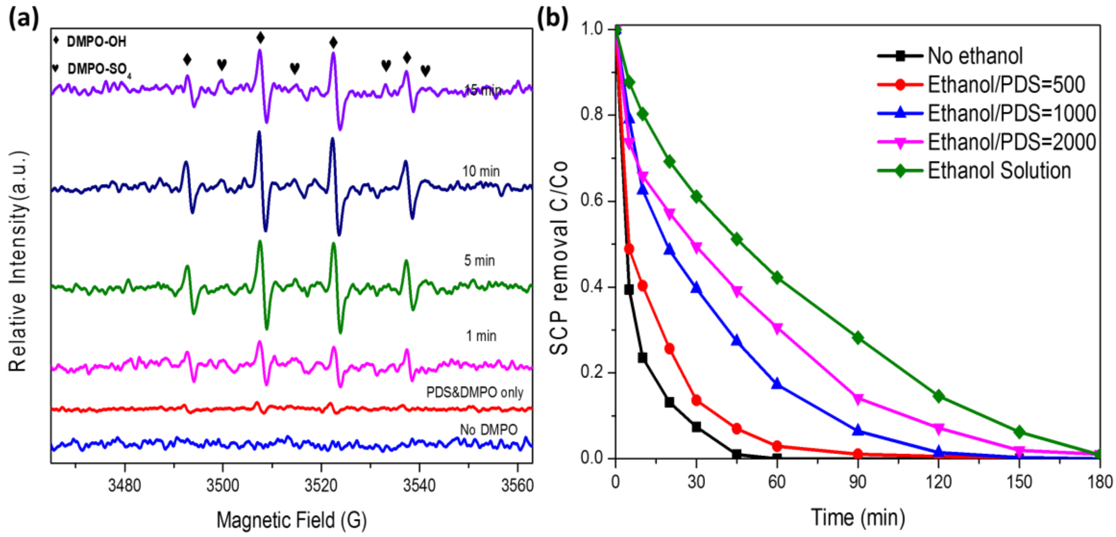

Fig. 8 (a) EPR spectra of PS activation with Ni@NCNT-800-3 different time intervals. (b) Effect of radical quenching on SCP degradation.

Other tests for identification of reactive species were also carried out. Degradation of furfuryl alcohol (FFA) as a $^1O_2$ probe compound was conducted (Fig. S13a). As shown, 11% of 20 ppm of FFA was removed after 3 h, suggesting that singlet oxygen provides a contribution to SCP degradation. Further quenching tests by using tert-butanol (TBA) and NaN_3 for hydroxyl radical and singlet oxygen, respectively, were conducted (Fig. S13b). In the presence of the two quenchers, SCP degradation was reduced, suggesting the contributions of hydroxyl radical and singlet oxygen in SCP degradation.

In our previous studies, a series of catalysts were carried out on controlled quenching experiments, cobalt oxide (Co_3O_4) and carbon nanotubes (CNT) were showing harsh catalytic decreasing after ethanol was presented in the solution and the organic degradation was totally prevented when all water was substituted to ethanol [30]. In contrast, nitrogen doped carbon nanotubes (N-CNT) displayed a minor influence from ethanol and maintained good oxidation efficiency even in ethanol solution. It was reported that the sp^2 carbon network can be activated for a better catalytic activity through conjugation with the lone-pair electrons of N atoms, thus, the activated electrons would work together with PS to react with the adsorbed SCP molecules [26][34]. As a result, the co-existing radical and non-radical reactions in Ni@NCNTs/PS system would accelerate the completion of SCP decomposition. From the experiments above and the previous studies, the possible mechanism of Ni@NCNTs/PS activation system is illustrated in **Fig. 9**.

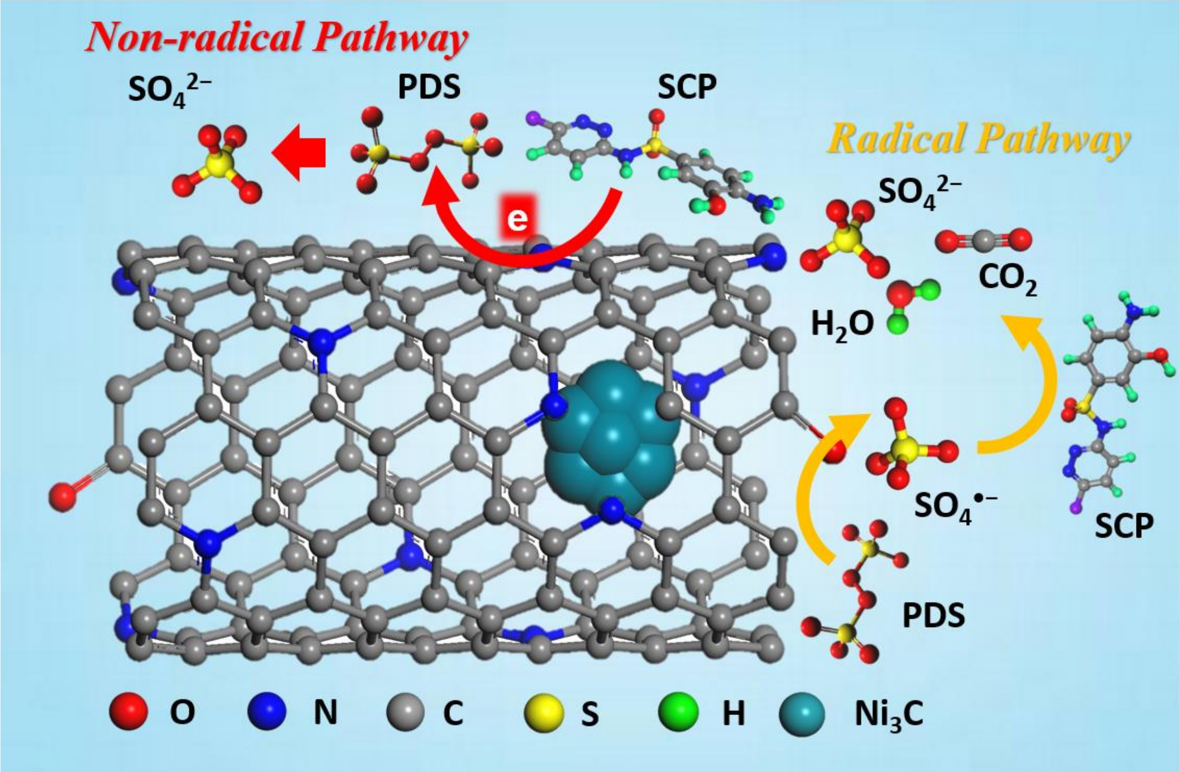

Fig. 9 Possible reaction mechanism for organic SCP oxidation by the Ni@NCNTs/PS system.

4. Conclusions

Ni@NCNTs was synthesized by a simple pyrolysis method. The fabrication conditions such as pyrolysis temperature and N precursor loading were closely related to the morphologies and catalysis of Ni@NCNTs. It was observed that the Ni@NCNTs was optimally prepared at 800 °C showing the most well-defined regular bamboo-like configuration and outstanding catalysis. The heterogeneous system of Ni@NCNTs and PS was applied for SCP removal, showing efficient adsorption capacity and oxidation efficiency. The effects of reaction temperature, solution pH, PS dosage on the reaction were in detail investigated, indicating the oxidation reaction was effective in a wide pH range and could be improved by increasing reaction temperature and PS amount at a controlled level. The mechanistic study demonstrated that the promoted adsorption and catalytic performances of Ni@NCNTs could be attributed to the unique nanotube morphology and the doping of nitrogen atoms, which acted as active sites for both the SCP adsorption and PS activation. In addition, the synergistic effect of N doping and Ni encapsulation enables Ni@NCNTs to present an excellent stability for reuse. The mechanistic insight of catalytic reaction for PS activation was investigated by EPR and quenching experiments, showing that radical ($SO_4^{-\bullet}$ and $^{\bullet}OH$) and non-radical reactions were involved in the activation processes.

Acknowledgments

We here thank Australian Research Council for their financial supporting under the project DP150103026 and as well as BHP Billiton for providing PhD scholarship. The authors also acknowledge the Curtin University Electron Microscope Facility partially funded by the University, State, and Commonwealth Governments for providing the equipment, scientific and technical assistance.

Appendix A. Supplementary data

Supplementary data associated with this article can be found, in the online version, at

References

[1] S.D. Richardson, S.Y. Kimura, Water analysis: Emerging contaminants and current issues, Analytical Chemistry 88 (2016) 546-582.

[2] B. Sun, M. Sato, J.S. Clements, Oxidative processes occurring when pulsed high voltage discharges degrade phenol in aqueous solution, Environmental Science & Technology 34 (2000) 509-513.

[3] S.A. Snyder, P. Westerhoff, Y. Yoon, D.L. Sedlak, Pharmaceuticals, personal care products, and endocrine disruptors in water: Implications for the water industry, Environmental Engineering Science 20 (2003) 449-469.

[4] F.C. Cabello, Heavy use of prophylactic antibiotics in aquaculture: a growing problem for human and animal health and for the environment, Environmental Microbiology 8 (2006) 1137-1144.

[5] H. Gold, Anthrax: A review of sixty cases, with a report on the therapeutic use of sulfonamide compounds, Archives of Internal Medicine 70 (1942) 785-821.

[6] R. F.Bevill, Sulfonamide residues in domestic animals, Journal of Veterinary Pharmacology and Therapeutics 12 (1989) 241-252.

[7] K. Kümmerer, Significance of antibiotics in the environment, Journal of Antimicrobial Chemotherapy 52 (2003) 5-7.

[8] A. Göbel, C.S. McArdell, M.J.F. Suter, W. Giger, Trace Determination of macrolide and sulfonamide antimicrobials, a human sulfonamide metabolite, and trimethoprim in wastewater using liquid chromatography coupled to electrospray tandem mass spectrometry, Analytical Chemistry 76 (2004) 4756-4764.

[9] F. Ingerslev, B. Halling-Sørensen, Biodegradability properties of sulfonamides in activated sludge, Environmental Toxicology and Chemistry 19 (2000) 2467-2473.

[10] W. Baran, E. Adamek, J. Ziemiańska, A. Sobczak, Effects of the presence of sulfonamides in the environment and their influence on human health, Journal of Hazardous Materials 196 (2011) 1-15.

[11] A. Göbel, C.S. McArdell, A. Joss, H. Siegrist, W. Giger, Fate of sulfonamides, macrolides, and trimethoprim in different wastewater treatment technologies, Science of the Total Environment 372 (2007) 361-371.

[12] A. Joss, E. Keller, A.C. Alder, A. Göbel, C.S. McArdell, T. Ternes, H. Siegrist, Removal of pharmaceuticals and fragrances in biological wastewater treatment, Water Research 39 (2005) 3139-3152.

[13] Y. Yang, J.J. Pignatello, J. Ma, W.A. Mitch, Comparison of halide impacts on the efficiency of contaminant degradation by sulfate and hydroxyl radical-based advanced oxidation processes (AOPs), Environmental Science & Technology 48 (2014) 2344-2351.

[14] E. Neyens, J. Baeyens, A review of classic Fenton's peroxidation as an advanced oxidation technique, Journal of Hazardous Materials 98 (2003) 33-50.

[15] S. Wang, A comparative study of Fenton and Fenton-like reaction kinetics in decolourisation of wastewater, Dyes and Pigments 76 (2008) 714-720.

[16] L. Hu, X. Yang, S. Dang, An easily recyclable Co/SBA-15 catalyst: Heterogeneous activation of peroxymonosulfate for the degradation of phenol in water, Applied Catalysis B: Environmental 102 (2011) 19-26.

[17] S.B. Hammouda, F. Zhao, Z. Safaei, V. Srivastava, D. Lakshmi Ramasamy, S. Iftekhar, S. kalliola, M. Sillanpää, Degradation and mineralization of phenol in aqueous medium by heterogeneous monopersulfate activation on nanostructured cobalt based-perovskite catalysts $ACoO_3$ (A=La, Ba, Sr and Ce): Characterization, kinetics and mechanism study, Applied Catalysis B: Environmental 215 (2017) 60-73.

[18] G.P. Anipsitakis, D.D. Dionysiou, Degradation of organic contaminants in water with sulfate radicals generated by the conjunction of peroxymonosulfate with cobalt, Environmental Science & Technology 37 (2003) 4790-4797.

[19] Y. Wang, H. Sun, H.M. Ang, M.O. Tadé, S. Wang, 3D-hierarchically structured MnO_2 for catalytic oxidation of phenol solutions by activation of peroxymonosulfate: Structure dependence and mechanism, Applied Catalysis B: Environmental 164 (2015) 159-167.

[20] E. Saputra, S. Muhammad, H. Sun, H.M. Ang, M.O. Tadé, S. Wang, Different crystallographic one-dimensional MnO_2 nanomaterials and their superior performance in catalytic phenol degradation, Environmental Science & Technology 47 (2013) 5882-5887.

[21] P. Hu, M. Long, Cobalt-catalyzed sulfate radical-based advanced oxidation: A review on heterogeneous catalysts and applications, Applied Catalysis B: Environmental 181 (2016) 103-117.

[22] P. Hu, M. Long, X. Bai, C. Wang, C. Cai, J. Fu, B. Zhou, Y. Zhou, Monolithic cobalt-doped carbon aerogel for efficient catalytic activation of peroxymonosulfate in water, Journal of Hazardous Materials 332 (2017) 195-204.

[23] S. Wang, H. Sun, H.M. Ang, M.O. Tadé, Adsorptive remediation of environmental pollutants using novel graphene-based nanomaterials, Chemical Engineering Journal 226 (2013) 336-347.

[24] T. Liu, Y. Li, Q. Du, J. Sun, Y. Jiao, G. Yang, Z. Wang, Y. Xia, W. Zhang, K. Wang, H. Zhu, D. Wu, Adsorption of methylene blue from aqueous solution by graphene, Colloids and Surfaces B: Biointerfaces 90 (2012) 197-203.

[25] D. Lin, B. Xing, Adsorption of phenolic compounds by carbon nanotubes: Role of aromaticity and substitution of hydroxyl groups, Environmental Science & Technology 42 (2008) 7254-7259.

[26] W. Tian, H. Zhang, X. Duan, H. Sun, M.O. Tade, H.M. Ang, S. Wang, Nitrogen- and sulfur-codoped hierarchically porous carbon for adsorptive and oxidative removal of pharmaceutical contaminants, ACS Applied Materials & Interfaces 8 (2016) 7184-7193.

[27] X. Duan, Z. Ao, H. Sun, S. Indrawirawan, Y. Wang, J. Kang, F. Liang, Z.H. Zhu, S. Wang, Nitrogen-doped graphene for generation and evolution of reactive radicals by metal-free catalysis, ACS Applied Materials & Interfaces 7 (2015) 4169-4178.

[28] Y. Wang, H. Sun, X. Duan, H.M. Ang, M.O. Tadé, S. Wang, A new magnetic nano zero-valent iron encapsulated in carbon spheres for oxidative degradation of phenol, Applied Catalysis B: Environmental 172-173 (2015) 73-81.

[29] H. Sun, Y. Wang, S. Liu, L. Ge, L. Wang, Z. Zhu, S. Wang, Facile synthesis of nitrogen doped reduced graphene oxide as a superior metal-free catalyst for oxidation, Chemical Communications 49 (2013) 9914-9916.

[30] X. Duan, H. Sun, Y. Wang, J. Kang, S. Wang, N-doping-induced nonradical reaction on single-walled carbon nanotubes for catalytic phenol oxidation, ACS Catalysis 5 (2015) 553-559.

[31] K. Gong, F. Du, Z. Xia, M. Durstock, L. Dai, Nitrogen-doped carbon nanotube arrays with high electrocatalytic activity for oxygen reduction, Science 323 (2009) 760-764.

[32] J. Kang, X. Duan, L. Zhou, H. Sun, M.O. Tadé, S. Wang, Carbocatalytic activation of persulfate for removal of antibiotics in water solutions, Chemical Engineering Journal 288 (2016) 399-405.

[33] X. Duan, H. Sun, J. Kang, Y. Wang, S. Indrawirawan, S. Wang, Insights into heterogeneous catalysis of persulfate activation on dimensional-structured nanocarbons, ACS Catalysis 5 (2015) 4629-4636.

[34] X. Duan, Z. Ao, L. Zhou, H. Sun, G. Wang, S. Wang, Occurrence of radical and nonradical pathways from carbocatalysts for aqueous and nonaqueous catalytic oxidation, Applied Catalysis B: Environmental 188 (2016) 98-105.

[35] Y. Wang, S. Indrawirawan, X. Duan, H. Sun, H.M. Ang, M.O. Tadé, S. Wang, New insights into heterogeneous generation and evolution processes of sulfate radicals for phenol degradation over one-dimensional α-MnO_2 nanostructures, Chemical Engineering Journal 266 (2015) 12-20.

[36] L. Qu, Y. Liu, J.-B. Baek, L. Dai, Nitrogen-doped graphene as efficient metal-free electrocatalyst for oxygen reduction in fuel cells, ACS Nano 4 (2010) 1321-1326.

[37] A. Ul-Hamid, A. Quddus, H. Saricimen, H. Dafalla, Corrosion behavior of coarse- and fine-grain Ni coatings incorporating $NaH_2PO_4.H_2O$ inhibitor treated substrates, Materials Research 18 (2015) 20-26.

[38] Y. Koltypin, A. Fernandez, T.C. Rojas, J. Campora, P. Palma, R. Prozorov, A. Gedanken, Encapsulation of nickel nanoparticles in carbon obtained by the sonochemical decomposition of $Ni(C_8H_{12})_2$, Chemistry of Materials 11 (1999) 1331-1335.

[39] J. Yuan, Y. Zhu, L. Li, Highly efficient bimetal synergetic catalysis by a multi-wall carbon nanotube supported palladium and nickel catalyst for the hydrogen storage of magnesium hydride, Chemical Communications 50 (2014) 6641-6644.

[40] M.A. Pimenta, G. Dresselhaus, M.S. Dresselhaus, L.G. Cancado, A. Jorio, R. Saito, Studying disorder in graphite-based systems by Raman spectroscopy, Physical Chemistry Chemical Physics 9 (2007) 1276-1290.

[41] C. Cong, T. Yu, H. Wang, Raman study on the g mode of graphene for determination of edge orientation, ACS Nano 4 (2010) 3175-3180.

[42] W.H. Organization, Guidelines for drinking-water quality - Volume 1: Recommendations, 2008.

[43] C.H. Kiang, M. Endo, P.M. Ajayan, G. Dresselhaus, M.S. Dresselhaus, Size effects in carbon nanotubes, Physical Review Letters 81 (1998) 1869-1872.

[44] R. Sen, B. C. Satishkumar, A. Govindaraj, K. R. Harikumar, M. K. Renganathan, C. N. R. Rao, Nitrogen-containing carbon nanotubes, Journal of Materials Chemistry 7 (1997) 2335-2337.

[45] Z.-H. Sheng, L. Shao, J.-J. Chen, W.-J. Bao, F.-B. Wang, X.-H. Xia, Catalyst-free synthesis of nitrogen-doped graphene via thermal annealing graphite oxide with melamine and its excellent electrocatalysis, ACS Nano 5 (2011) 4350-4358.

[46] D. Deng, X. Pan, L. Yu, Y. Cui, Y. Jiang, J. Qi, W.-X. Li, Q. Fu, X. Ma, Q. Xue, G. Sun, X. Bao, Toward N-doped graphene via solvothermal synthesis, Chemistry of Materials 23 (2011) 1188-1193.

[47] J. Long, X. Xie, J. Xu, Q. Gu, L. Chen, X. Wang, Nitrogen-doped graphene nanosheets as metal-free catalysts for aerobic selective oxidation of benzylic alcohols, ACS Catalysis 2 (2012) 622-631.

[48] X. Li, H. Wang, J.T. Robinson, H. Sanchez, G. Diankov, H. Dai, Simultaneous nitrogen doping and reduction of graphene oxide, Journal of the American Chemical Society 131 (2009) 15939-15944.

[49] K. Kinoshita, Carbon: electrochemical and physicochemical properties, John Wiley Sons,New York, 1988.

[50] J. Lee, J. Kim, T. Hyeon, Recent progress in the synthesis of porous carbon materials, Advanced Materials 18 (2006) 2073-2094.

[51] J. Zhang, X. Liu, R. Blume, A. Zhang, R. Schlögl, D.S. Su, Surface-modified carbon nanotubes catalyze oxidative dehydrogenation of butane, Science 322 (2008) 73-77.

[52] G. Zhong, H. Wang, H. Yu, F. Peng, Nitrogen doped carbon nanotubes with encapsulated ferric carbide as excellent electrocatalyst for oxygen reduction reaction in acid and alkaline media, Journal of Power Sources 286 (2015) 495-503.

[53] B. Frank, J. Zhang, R. Blume, R. Schlögl, D.S. Su, Heteroatoms increase the selectivity in oxidative dehydrogenation reactions on nanocarbons, Angewandte Chemie International Edition 48 (2009) 6913-6917.

[54] P.R. Shukla, S. Wang, H. Sun, H.M. Ang, M. Tadé, Activated carbon supported cobalt catalysts for advanced oxidation of organic contaminants in aqueous solution, Applied Catalysis B: Environmental 100 (2010) 529-534.

[55] P. Shukla, H. Sun, S. Wang, H.M. Ang, M.O. Tadé, Co-SBA-15 for heterogeneous oxidation of phenol with sulfate radical for wastewater treatment, Catalysis Today 175 (2011) 380-385.

[56] P. Shukla, H. Sun, S. Wang, H.M. Ang, M.O. Tadé, Nanosized Co_3O_4/SiO_2 for heterogeneous oxidation of phenolic contaminants in waste water, Separation and Purification Technology 77 (2011) 230-236.

[57] Y. Wang, H. Sun, H.M. Ang, M.O. Tadé, S. Wang, Magnetic Fe_3O_4/carbon sphere/cobalt composites for catalytic oxidation of phenol solutions with sulfate radicals, Chemical Engineering Journal 245 (2014) 1-9.

[58] Y. Ji, C. Ferronato, A. Salvador, X. Yang, J.-M. Chovelon, Degradation of ciprofloxacin and sulfamethoxazole by ferrous-activated persulfate: Implications for remediation of groundwater contaminated by antibiotics, Science of the Total Environment 472 (2014) 800-808.

[59] Y. Ji, Y. Fan, K. Liu, D. Kong, J. Lu, Thermo activated persulfate oxidation of antibiotic sulfamethoxazole and structurally related compounds, Water Research 87 (2015) 1-9.

[60] X. Duan, C. Su, L. Zhou, H. Sun, A. Suvorova, T. Odedairo, Z. Zhu, Z. Shao, S. Wang, Surface controlled generation of reactive radicals from persulfate by carbocatalysis on nanodiamonds, Applied Catalysis B: Environmental 194 (2016) 7-15.